



ELSEVIER

Contents lists available at ScienceDirect

Planetary and Space Science

journal homepage: www.elsevier.com/locate/pss

Radius and limb topography of Mercury obtained from images acquired during the MESSENGER flybys

Jürgen Oberst^{a,*}, Stephan Elgner^a, F. Scott Turner^b, Mark E. Perry^b, Robert W. Gaskell^c, Maria T. Zuber^d, Mark S. Robinson^e, Sean C. Solomon^f

^a German Aerospace Center, Institute of Planetary Research, Rutherfordstr. 2, D-12489 Berlin, Germany

^b Johns Hopkins University Applied Physics Laboratory, 11100 Johns Hopkins Road, Laurel, MD 20723, USA

^c Planetary Science Institute, 1700 East Fort Lowell, Suite 106, Tucson, AZ 85719, USA

^d Department of Earth, Atmospheric, and Planetary Sciences, Massachusetts Institute of Technology, Cambridge, MA 02139, USA

^e School of Earth and Space Exploration, Arizona State University, Tempe, AZ 85287, USA

^f Department of Terrestrial Magnetism, Carnegie Institution of Washington, Washington, DC 20015, USA

ARTICLE INFO

Article history:

Received 23 December 2010

Received in revised form

26 June 2011

Accepted 1 July 2011

Keywords:

Mercury

Radius

Topography

Imaging

MESSENGER

ABSTRACT

Analysis of images obtained by the MESSENGER spacecraft during its three flybys of Mercury yields a new estimate for the planet's mean radius of 2439.25 ± 0.69 km, in agreement with results from Mariner 10 and Earth-based observations, as well as with MESSENGER altimeter and occultation data. The mean equatorial radius and polar radius are identical to within error, suggesting that rotational oblateness is negligible when compared with other sources of topography. This result is consistent with the small gravitational oblateness of the planet. Minor differences in radius obtained at different locations reflect regional variations in topography. Residual topography along three limb profiles has a dynamic range of 7.4 km and a root-mean-square roughness of 0.8 km over hemispherical scales. Following MESSENGER's entry into orbit about Mercury in March 2011, we expect considerable additional improvements to our knowledge of Mercury's size and shape.

© 2011 Elsevier Ltd. All rights reserved.

1. Introduction

The size and shape of a planet constitute basic information for geodetic and cartographic studies. Unfortunately, these fundamental data are still limited for Mercury, the least explored among the terrestrial planets. From early optical observations, de Vaucouleurs (1964) reported a mean radius for Mercury of approximately 2440 km. From early Earth-based radar data, Ash et al. (1971) obtained a mean equatorial radius of 2439 ± 1 km, and subsequent radar observations yielded the value 2440 ± 1 km (Harmon et al., 1986; Harmon and Campbell, 1988). Occultations of the radio-tracking signal from the Mariner 10 spacecraft during its first Mercury flyby in 1974 provided precise estimates of Mercury's radius at two locations (Howard et al., 1974; Fjeldbo et al., 1976). No occultations were observed during Mariner 10's second or third Mercury encounters. Moreover, no direct measurements of the planet's radius derived from Mariner 10 images were reported, most likely because full-disk images of Mercury were at low resolution. Also, the Mariner 10 vidicon cameras suffered from image distortions, which required extensive geometric calibration

procedures (Davies and Batson, 1975; Robinson et al., 1999) and which therefore could not improve on the accuracy of previous radius measurements.

More recently, Anderson et al. (1996) revisited radar data spanning the years from 1966 to 1974 as well as new data obtained during 1974–1990. Their analysis of 629 radius residuals from different rotational phase angles suggested that the shape of Mercury can be approximated by an ellipsoidal model slightly offset with respect to the planet's center of mass (see below). Because Mercury's orbital and equatorial planes are within 7° of the ecliptic, the radar determinations of radius data are restricted to near-equatorial areas, thus leaving the polar radius of the planet poorly constrained.

During its three flybys of Mercury (Solomon et al., 2007, 2008), the MERCURY Surface, Space ENVIRONMENT, GEOchemistry, and Ranging (MESSENGER) spacecraft obtained new data on Mercury's size and shape. Laser altimeter profiles obtained during the first and second flybys (M1 and M2, respectively) provided a means to derive the long-wavelength shape of a portion of Mercury's equatorial region (Zuber et al., 2008; Smith et al., 2010). Radio occultations observed during M1 and MESSENGER's third flyby (M3) added further constraints to the determination of Mercury's near-equatorial radius (Perry et al., this issue). A summary of all prior determinations of the radius of Mercury is given in Table 1.

* Corresponding author. Tel.: +49 30 67055 336.

E-mail address: Juergen.Oberst@dlr.de (J. Oberst).

Table 1
Estimates of the size and shape of Mercury.

Method	Value	Reference
Optical	2440.0 ± 7.5 km	de Vaucouleurs (1964)
Early radar (equatorial only)	2439.0 ± 1.0 km	Ash et al. (1971)
Mariner 10 occultations		Fjeldbo et al. (1976)
Ingress (1.1°N, 67.4°E)	2439.5 ± 1.0 km	
Egress (67.6°N 258.4°E)	2439.0 ± 1.0 km	
Radar (equatorial only) (currently IAU-recommended ^a)	2439.7 ± 1.0 km	Harmon and Campbell (1988)
Radar		Anderson et al. (1996)
<i>a</i> (semi-major axis of equatorial shape)	2440.6 ± 0.1 km	
<i>b</i> (semi-minor axis of equatorial shape)	2439.3 ± 0.1 km	
<i>c</i> (polar radius)	2432.9 ± 8.8 km	
MESSENGER		
Laser altimetry		Smith et al. (2010)
<i>a</i> – <i>b</i>	1.6 km	
Occultations		Perry et al. (this issue)
M1 ingress (25.54°S, 225.28°E)	2437.3 ± 0.35 km	
M1 egress (7.33°S, 41.83°E)	2439.9 ± 0.35 km	
M3 egress (36.06°N, 28.23°E)	2440.5 ± 0.35 km	
Stereo topographic models		Preusker et al. (this issue)
<i>r</i> (mean radius)	2440.3 km	
Limb fits		This study
<i>r</i> (mean radius)	2439.25 ± 0.69 km	

^a Davies et al. (1989), Archinal et al. (2010).

In this paper we present new estimates for Mercury’s radius from the analysis of MESSENGER images of the planetary limb. Central to this work are images obtained with MESSENGER’s Mercury Dual Imaging System (MDIS) (Hawkins et al., 2007). MDIS obtained full-planet images of Mercury showing equatorial and polar radii alike on approach and departure during each of the three flybys. MDIS is equipped with charge-coupled device (CCD) sensors, which are known to produce images of reproducible geometric properties that can be measured and calibrated. MDIS also features a passive thermal design that renders the instrument nearly mechanically invariant to changing thermal conditions, which ensures geometrical stability. Moreover, the optical performance of the wide-angle camera on MDIS is insensitive to thermal changes over the instrument’s operational temperature range (Hawkins et al., 2007). Hence, accurate estimates of Mercury’s radius can be expected from the application of photogrammetric analysis techniques.

2. MDIS camera and geometric calibration

2.1. Cameras

MDIS consists of a wide-angle camera (WAC) and a narrow-angle camera (NAC), both mounted on a pivot platform and co-aligned (Hawkins et al., 2007). The two cameras are equipped with identical 1024 × 1024-format CCDs featuring 14-μm pixels. Images are quantized to 12 bits and are often converted to 8 bits for data compression. Images can also be reduced to 512 × 512 by binning during read-out or with the onboard data processing unit. The WAC, utilized in this study, is equipped with a 12-position filter wheel that has 11 narrow-band spectral filters and one panchromatic “clear” filter, intended for imaging of star fields and optical navigation.

2.2. Geometric calibration

Images were corrected for geometric distortions introduced by the camera’s optical system. Precise knowledge of focal length and

geometric calibration is crucial to the proper scaling of the images. Although the MESSENGER team has been examining a variety of geometric calibrations (Hawkins et al., 2007, 2009), this study uses a geometric distortion model that includes radial and tangential distortion (Brown, 1971) as well as distortion effects of higher order (see Appendix for details). The unknown parameters in the calibration model were determined by in-flight star calibrations. Typical images of the Pleiades star field taken by the panchromatic (B) filter of the WAC show 170–190 stars, the positions of which can be compared with star coordinates in the PPM star catalog (Röser and Bastian, 1991, 1993). The positional errors of stars in the PPM catalog are expected to be 0.02 pixels for the WAC over a time frame of 10 years. Star coordinates are measured at sub-pixel accuracy by fitting Gaussian functions to pixel patterns of the stars. A shortcoming for our calibration effort is the width of the point-spread function of the camera system (Hawkins et al., 2007), which limits the accuracy of image coordinates for fainter stars (approximately one-third) to one pixel.

We expect that the effective focal lengths for images taken with the different filters may differ. Unfortunately, images of the Pleiades star field taken with the narrow-band filters typically do not show more than 8–16 stars, unevenly distributed over the field of view, a number insufficient to conduct precise studies of the full geometric distortion parameter set. We have therefore assumed that the distortion parameters for images obtained with WAC filter B are valid for those taken with other WAC filters as well. However, effective focal lengths for each filter were derived independently.

We analyzed jointly 17 B-filter images of different star targets and pivot positions to ensure independence among individual data sets. In a combined least-squares fit, we estimated focal length as well as the set of distortion parameters for our calibration model (see Appendix). Residual errors of star coordinate measurements averaged 0.1 pixels. The focal length estimate of 78.202 ± 0.004 mm differs from the ground-determined focal length of 77.96 ± 0.15 mm but is in good agreement with the focal length of 78.16 ± 0.15 mm obtained during early in-flight calibrations (Hawkins et al., 2007). The remaining difference in focal length probably originates from differences in the distortion models that were used. The geometric distortion amounts to a maximum of 1.1 pixels near the lower left

Table 2
Focal lengths for WAC filters derived from analyses of Mercury surface control points.

Filter	Focal length (mm)
A	78.22164
C	78.05320
D	78.09631
E	78.13646
F	78.11253
G	78.23670
H	78.46714
I	78.52539
J	78.40472
K	78.52753
L	78.33067

Note: the standard deviation for each of these values is 0.002 mm.

Table 3
Mercury limb images used in this analysis.

M1 approach	M2 approach	M3 approach
EW0108820007C	EW0131764500C	EW0162741039C
EW0108820012D	EW0131764505D	EW0162741043D
EW0108820017E	EW0131764510E	EW0162741047E
EW0108820022F	EW0131764515F	EW0162741051F
EW0108820027G	EW0131764520G	EW0162741055G
EW0108820032H	EW0131764525H	EW0162741059H
EW0108820037I	EW0131764530I	EW0162741063I
EW0108820042J	EW0131764535J	EW0162741067J
EW0108820047K	EW0131764540K	EW0162741071K
EW0108820052L	EW0131764545L	EW0162741075L
EW0108820057A	EW0131764550A	EW0162741079A
	EW0162741083B	
M1 departure	M2 departure	
EW0108829678A	EW0131775228A	
EW0108829683L	EW0131775232L	
EW0108829688K	EW0131775236K	
EW0108829693J	EW0131775240J	
EW0108829698I	EW0131775244I	
EW0108829703H	EW0131775248H	
EW0108829708G	EW0131775252G	
EW0108829713F	EW0131775256F	
EW0108829718E	EW0131775260E	
EW0108829723D	EW0131775264D	
EW0108829728C	EW0131775268C	
	EW0131775283B	

Note: see <http://pds-imaging.jpl.nasa.gov> for further information on MESSENGER images.

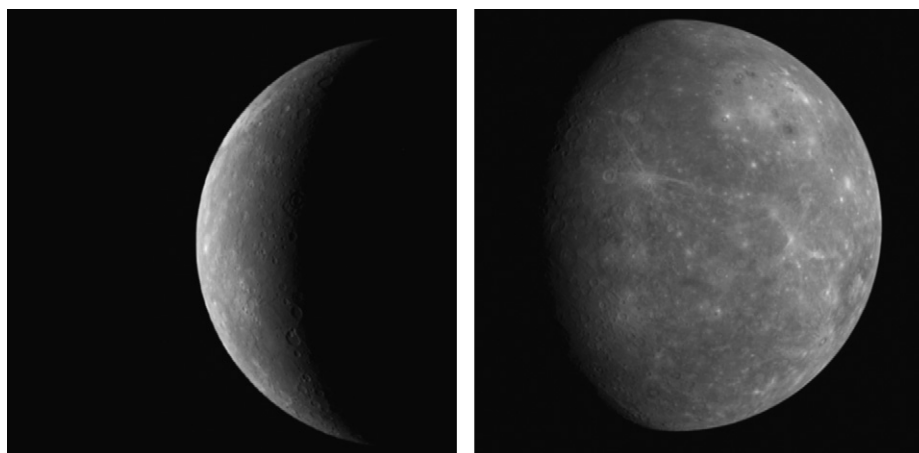


Fig. 1. WAC approach (EW0108820057A, left) and departure (EW0108829678A, right) images taken during M1. The resolution at the limb at this distance (30,000 km) is 5.3 km/pixel. North is up.

image corner, demonstrating the importance of image distortion corrections for precise photogrammetric measurements. Unfortunately, the well-calibrated panchromatic filter B is of only limited use for limb imaging, as images acquired through this filter develop CCD-saturation-induced smearing effects due to overexposure when targeting the bright Mercury disk, even at minimum exposure times.

A set of focal lengths for images obtained with WAC filters A and C–L was derived by matching WAC to NAC images of Mercury's surface (Table 2). The WAC focal lengths, including distortion, were determined by minimizing the difference between predicted and observed image locations of control points. The three-dimensional coordinates of more than 21,000 control points, identified in 1540 WAC and NAC images, were determined. The solution was constrained by more than 1.1 million measurement pairs.

3. Limb fitting

3.1. Method

Shape parameters for Mercury were modeled on the basis of limb observations, following methods described by Thomas (1993) and Thomas et al. (2005).

3.2. Acquiring limb coordinates

The determination of the sub-pixel image coordinates of limb positions was made with a standard software tool (<http://www-mipl.jpl.nasa.gov/external/vicar.html>), which applies a contrast-based search along the predicted limb positions. Typically, 750 and 900 limb points were found from the selected

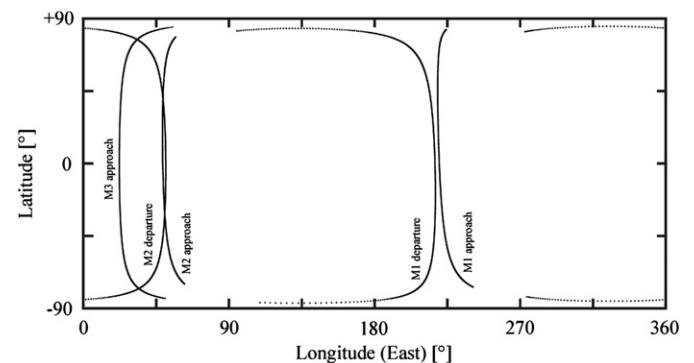


Fig. 2. Mercury limb positions at the times of the three MESSENGER flybys.

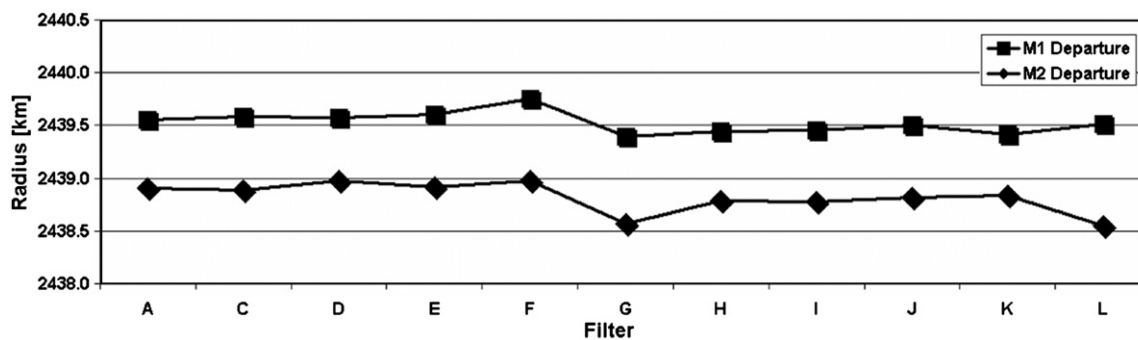


Fig. 3. Estimates of radius from limb observations made with the individual WAC color filters on departure during M1 and M2. Values show good agreement and demonstrate that the different focal lengths for the filters are internally consistent.

Table 4
Radius determinations from limb observations during the MESSENGER flybys.

	Radius (km)	
M1 approach	2439.82	± 0.10
M1 departure	2439.52	± 0.10
M2 approach	2438.52	± 0.08
M2 departure	2438.82	± 0.15
M3 approach	2438.61	± 0.06
All data	2439.25	± 0.69

approach and departure images, taken under high and low phase angles, respectively. The acquired limb points were inspected to eliminate misidentified points at the terminator.

3.3. Creating nominal limbs

Software tools have been developed that make heavy use of subroutines from the spacecraft, planet, instrument, C-matrix, and events (SPICE) software toolkit (<http://naif.jpl.nasa.gov/naif/toolkit.html>) to predict the Mercury limb positions in the images, given spacecraft position, camera pointing direction, and a three-axis shape model for Mercury. The WAC geometric distortion model was implemented in the tool. Coordinate pairs of limb points were found by creating vector arrays originating from the proposed center of figure in the image to points on the actual limb from high to low latitudes.

3.4. Limb fit

Camera pointing and Mercury shape parameters were treated as unknowns to be determined as part of the limb-fit solution. Either a single radius, two spheroid radii, or three ellipsoid radii can be determined. As full shape parameters cannot be determined from single limb profiles, several images from different flight phases were processed in a single adjustment. By combining several images, the effect of local topography is reduced. Weights p_i were applied to emphasize images from close range with good limb resolution, where

$$p_i = \frac{d_{\min}^2}{d_i^2} \quad (1)$$

and where d_i is the distance to Mercury for the i th image and d_{\min} is the minimum distance among all images. Several available far-range images that did not offer any improvements in results but markedly increased computation time were not included. An

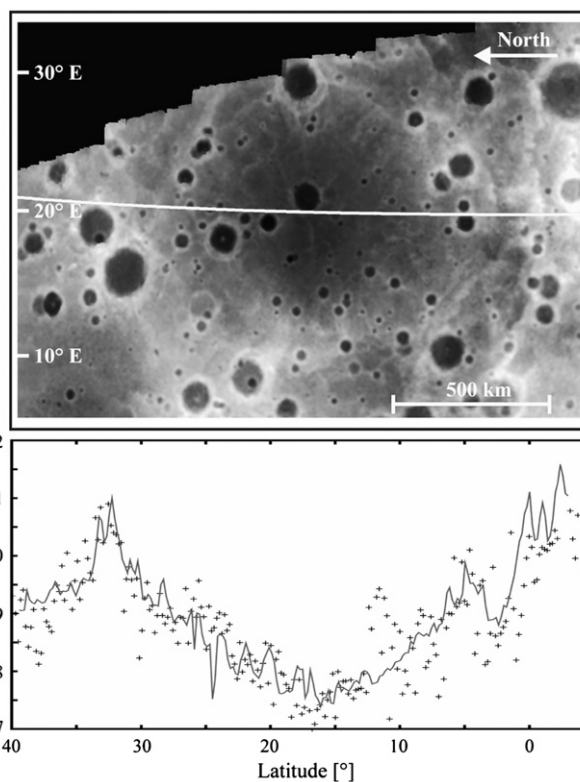


Fig. 4. Limb profile from M3 (plus symbols) compared with the profile (solid line) from a digital terrain model (DTM), derived from MESSENGER stereo images (top panel), featuring what may be among the largest impact basins on Mercury, approximately 1500 km in diameter and 2.5 km in depth (Preusker et al., this issue). The DTM is in a cylindrical equidistant projection. The large-scale topography from the limb profile and the DTM (bottom panel) show generally good agreement.

iterative least-squares method was used to fit the limb model to the actual limb data.

4. Limb images

Images of the full planetary limb were captured on approach and departure during the three Mercury flybys (see Table 3 for an image list). We concentrated on full-color sequences obtained from ranges of about 30,000 km, at which Mercury fills the WAC field of view to 90% (Fig. 1). Because MESSENGER entered safe-mode near closest approach during the third flyby, only

inbound images are available from that encounter. Because the longitudes at closest approach for the second and third flybys were similar and because the first and second flybys were nearly on opposite hemispheres of the planet (Fig. 2), we did not have sufficient data to determine Mercury's equatorial ellipticity.

5. Limb-fitting results

5.1. Results for different filters

Results for different filters were compared to verify that the focal length estimates resulted in comparable values of radius. Though some small systematic trends among the absolute values of the focal lengths remain, we find good agreement for radius data from filter to filter to within ± 0.1 km on average for each spacecraft trajectory leg (Fig. 3).

5.2. Average Mercury radius

Radius estimates obtained with the WAC filters show consistent results from approach and departure images for each individual flyby (Table 4), which is expected inasmuch as the limbs during approach and departure are at similar longitudes. From results obtained during the first flyby, Mercury's radius is

$r=2439.67 \pm 0.18$ km, where the error is the standard deviation obtained from the results for individual filters.

Results from the second flyby give a significantly smaller value for the radius, at an average value of $r=2438.67 \pm 0.19$ km. From third flyby results we obtained $r=2438.61 \pm 0.06$ km, which matches the value from the second flyby, for which limb positions are similar.

From an analysis that incorporated data from all three flybys, we obtain a radius of $r=2439.25 \pm 0.69$ km.

The root-mean-squared (RMS) error after the fit is about ± 0.76 km for the first and second flybys, with slightly lower values for the departure than for the approach images, and ± 0.88 km for the third. These numbers are relatively consistent among results from individual filters, so we may presume that topography is the main contributor to these differences in average values.

5.3. Polar and equatorial radii

Next, we solved separately for the mean equatorial radius, r_{eq} , and the polar radius, r_{pol} . As approach images have shorter limb arcs and do not cover areas near the poles, only departure images were used in the analysis. We found that the difference between the values for equatorial and polar radius is not significant. On average, we estimate $r_{eq} - r_{pol} = 0.00 \pm 0.01$ km. With the limited

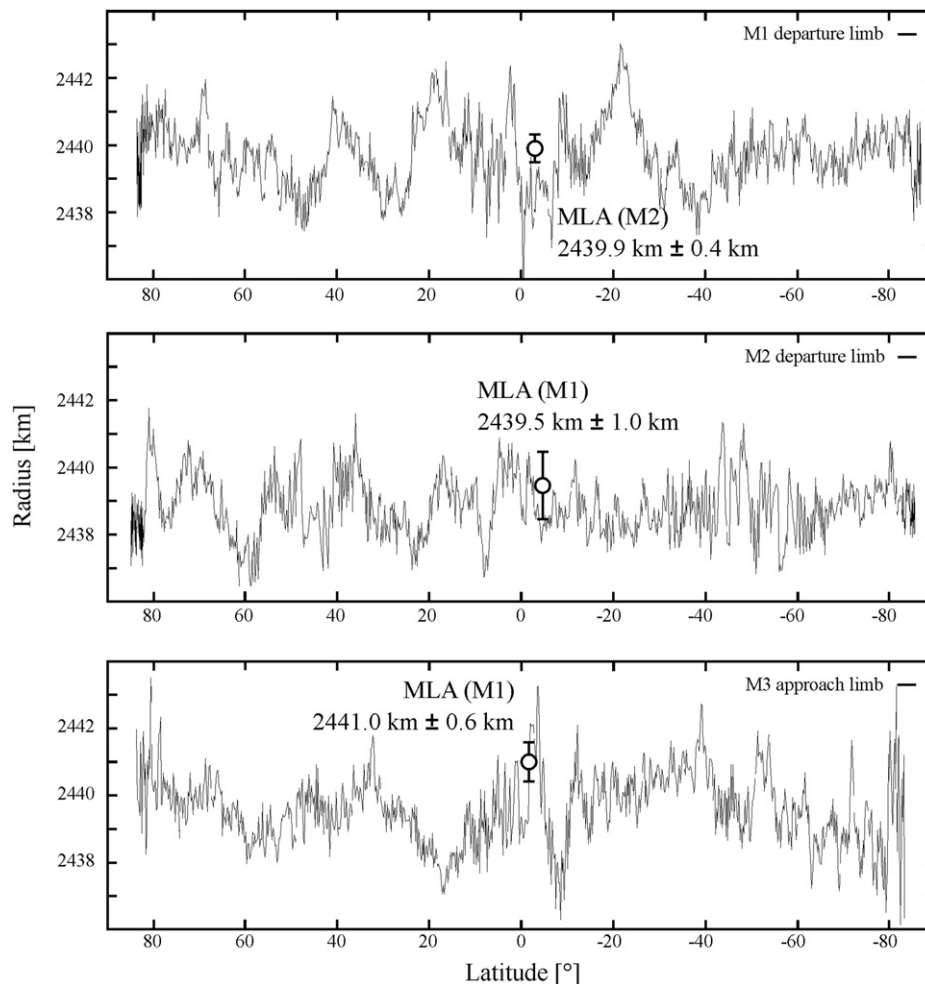


Fig. 5. Comparison of limb profiles and topography from MLA at crossover points. MLA heights are averaged over an along-track distance of 50 km; error bars show one standard deviation over that averaging distance.

coverage of limb positions during the flybys (Fig. 2), we cannot solve for equatorial ellipticity.

5.4. Limb residuals and topography

The residuals after the fits were examined to assess variations in topography along the limb profiles. As the images were taken from spacecraft positions near Mercury's equatorial plane, the limb profiles essentially extend from high northern to high southern latitudes with negligible differences in longitude for the images during a given approach or departure sequence.

The total dynamic range of the limb residuals was measured at 6.1 km during M1, 5.3 km during M2, and 7.4 km during M3. The total RMS residual was approximately 0.16 pixels, or 0.79 km (with an image resolution of approximately 5.3 km/pixel for the WAC at a range of 30,000 km). This value may be compared with the RMS roughness of 0.93 km obtained from the M1 laser altimeter profile over a similar length scale (Zuber et al., 2008) and an RMS roughness of 0.6 km from stereo topographic models (Preusker et al., this issue).

Efforts were made to find correlations between patterns in the limb-fit residuals and features seen in MESSENGER stereo terrain models (Preusker et al., this issue). The limb view vectors are tangent to the planet radius vectors and can be modified by features in the foreground or background. For example, an object with an elevation of 0.8 km (the RMS of limb residuals) intersects the tangential vector at a distance of 45 km, or 1°, from the expected limb point. Notwithstanding this point, on the approach limb of M3, we identified a depression that is also seen in stereo terrain models (Preusker et al., this issue) and may mark a prominent 1500-km-diameter impact basin (Fig. 4).

5.5. Comparisons with MLA profiles

Topographic profiles obtained by the Mercury Laser Altimeter (MLA) (Cavanaugh et al., 2007) during M1 and M2 extend over a total range of longitudes of about 170° at low latitudes on opposite sides of the planet (Zuber et al., 2008; Smith et al., 2010) and thus run perpendicular to our limb profiles. Limb profiles from the three flybys and MLA profiles can be compared at their points of intersection. Height data at their intersection points were found to agree to within the short-wavelength variability in the MLA-derived elevations (Fig. 5).

6. Summary

From limb images obtained during the three MESSENGER flybys we have derived a new estimate for the radius of Mercury of 2439.25 ± 0.69 km. Moreover, we derived a new constraint on Mercury's polar radius, which previously was only poorly constrained. In particular, the polar radius derived from limb-height measurements is not resolvably different from the mean equatorial radius. Analysis of radio-tracking data from the MESSENGER flybys indicates that the gravitational oblateness of Mercury is also small in magnitude, i.e., the coefficient for the second-degree zonal component of the gravitational potential C_{20} derived from MESSENGER observations to date is -0.94×10^{-5} (Smith et al., 2010). For a uniform-density planet, this value of C_{20} is equivalent to a polar flattening $r_{\text{eq}} - r_{\text{pol}} = 35$ m (e.g., Montenbruck and Gill, 2000, p. 60), below our detection limit. Of course, Mercury does not have a uniform distribution of internal density, and there is likely to be a long-wavelength component to lithospheric support of topography. This comparison, although consistent with our findings, is thus an oversimplification.

MESSENGER will enter into orbit about Mercury in March 2011 and is expected to obtain precise shape parameters and a topographic map of the planet from a combination of laser altimetry in the northern hemisphere and global stereogrammetry. Further efforts will be made to capture radio occultations and limb images from orbit, particularly for areas in the southern hemisphere.

Acknowledgments

We thank Brent Archinal and an anonymous reviewer for comments and suggestions that helped improve an earlier version of this manuscript.

Appendix. WAC distortion model

The model for WAC distortion used here matches distortion patterns of the camera. It features a polynomial for radial distortion dr with three parameters (A_1 , A_2 , and A_3),

$$\begin{aligned} dr &= A_1 r^3 + A_2 r^5 + A_3 r^7 \\ dx_{\text{rad}} &= \frac{x dr}{r} \\ dy_{\text{rad}} &= \frac{y dr}{r} \end{aligned} \quad (2)$$

where x and y are coordinates in the image plane (in mm) and

$$r = \sqrt{(x-x_0)^2 + (y-y_0)^2} \quad (3)$$

where x_0 and y_0 are the coordinates of the principal point; polynomials with two parameters (B_1 and B_2) for radial-asymmetric and tangential distortion (Brown, 1971),

$$\begin{aligned} dx_{\text{tan}} &= 2B_2 xy + B_1(r^2 + 2x^2) \\ dy_{\text{tan}} &= 2B_1 xy + B_2(r^2 + 2y^2); \end{aligned} \quad (4)$$

one parameter each (C_1 and C_2 , respectively) for affinity and non-orthogonality (shear),

$$\begin{aligned} dx_{\text{aff}} &= C_1 x \\ dy_{\text{aff}} &= -C_1 y \end{aligned} \quad (5)$$

$$\begin{aligned} dx_{\text{shear}} &= C_2 y \\ dy_{\text{shear}} &= C_2 x; \end{aligned} \quad (6)$$

and four parameters (D_1 and D_2 , and E_1 and E_2 , respectively) to remove tilt and bending effects,

$$\begin{aligned} dx_{\text{tilt}} &= D_1 xy \\ dy_{\text{tilt}} &= D_2 xy \end{aligned} \quad (7)$$

$$\begin{aligned} dx_{\text{bend}} &= E_1 y^2 \\ dy_{\text{bend}} &= E_2 x^2. \end{aligned} \quad (8)$$

The individual distortion terms are subtracted from the image coordinates to correct for geometric distortion:

$$\begin{aligned} x_{\text{undistorted}} &= x - (dx_{\text{rad}} + dx_{\text{tan}} + dx_{\text{aff}} + dx_{\text{shear}} + dx_{\text{tilt}} + dx_{\text{bend}}) \\ y_{\text{undistorted}} &= y - (dy_{\text{rad}} + dy_{\text{tan}} + dy_{\text{aff}} + dy_{\text{shear}} + dy_{\text{tilt}} + dy_{\text{bend}}) \end{aligned} \quad (9)$$

Focal length and geometric distortion parameters are determined by least-squares fit (Table A1). The three camera pointing angles of the exterior orientation are considered to be unknown and are determined simultaneously during the fit. Because of a high correlation between orientation angles and principal point coordinates, the latter are considered as fixed in the fits. Therefore the principal point is assumed to coincide with the image center.

Table A1

Calibration model parameters and their standard deviations for WAC filter B.

Focal length	78.20234 mm	± 0.00402
A_1	1.346×10^{-5}	$\pm 3.79 \times 10^{-6}$
A_2	-2.278×10^{-7}	$\pm 8.39 \times 10^{-8}$
A_3	1.695×10^{-9}	$\pm 5.57 \times 10^{-10}$
B_1	-2.418×10^{-5}	$\pm 7.01 \times 10^{-7}$
B_2	6.038×10^{-7}	$\pm 7.56 \times 10^{-7}$
C_1	-5.487×10^{-5}	$\pm 9.61 \times 10^{-6}$
C_2	-5.117×10^{-5}	$\pm 8.64 \times 10^{-6}$
D_1	1.445×10^{-5}	$\pm 2.87 \times 10^{-6}$
D_2	-2.894×10^{-5}	$\pm 2.81 \times 10^{-6}$
E_1	2.456×10^{-5}	$\pm 2.72 \times 10^{-6}$
E_2	1.438×10^{-5}	$\pm 2.60 \times 10^{-6}$

References

- Anderson, J.D., Jurgens, R.F., Lau, E.L., Slade III, M.A., Schubert, G., 1996. Shape and orientation of Mercury from radar ranging data. *Icarus* 124, 690–697.
- Archinal, B.A., A'Hearn, M.F., Bowell, E., Conrad, A., Consolmagno, G.J., Courtin, R., Fukushima, T., Hestroffer, D., Hilton, J.L., Krasinsky, G.A., Neumann, G., Oberst, J., Seidelmann, P.K., Stooke, P., Tholen, D.J., Thomas, P.C., Williams, I.P., 2010. Report of the IAU Working Group on Cartographic Coordinates and Rotational Elements: 2009. *Celest. Mech. Dynam. Astron.* 109, 101–135.
- Ash, M.E., Shapiro, I.I., Smith, W.B., 1971. The system of planetary masses. *Science* 174, 551–556.
- Brown, D.C., 1971. Close-range camera calibration. *Photogramm. Eng.* 37, 855–866.
- Cavanaugh, J.F., Smith, J.C., Sun, X., Bartels, A.E., Ramos-Izquierdo, L., Krebs, D.J., McGarry, J.F., Trunzo, R., Novo-Gradac, A.M., Britt, J.L., Karsh, J., Katz, R.B., Lukemire, A.T., Szymkiewicz, R., Berry, D.L., Swinski, J.P., Neumann, G.A., Zuber, M.T., Smith, D.E., 2007. The Mercury Laser Altimeter instrument for the MESSENGER mission. *Space Sci. Rev.* 131, 451–479.
- Davies, M.E., Batson, R.M., 1975. Surface coordinates and cartography of Mercury. *J. Geophys. Res.* 80, 2417–2430.
- Davies, M.E., Abalakin, V.K., Bursa, M., Hunt, G.E., Lieske, J.H., 1989. Report of the IAU/IAG/COSPAR Working Group on Cartographic Coordinates and Rotational Elements of the Planets and Satellites: 1988. *Celest. Mech. Dynam. Astron.* 46, 187–204.
- de Vaucouleurs, G., 1964. Geometric and photometric properties of the terrestrial planets. *Icarus* 3, 187–235.
- Fjeldbo, G., Kliore, A., Sweetnam, D., Esposito, P., Seidel, B., Howard, T., 1976. The occultation of Mariner 10 by Mercury. *Icarus*, 439–444.
- Harmon, J.K., Campbell, D.B., 1988. Radar observations of Mercury. In: Vilas, F., Chapman, C.R., Matthews, M.S. (Eds.), *Mercury*. University of Arizona Press, Tucson, Ariz., pp. 101–117.
- Harmon, J.K., Campbell, D.B., Bindschadler, D.L., Head, J.W., Shapiro, I.I., 1986. Radar altimetry of Mercury—a preliminary analysis. *J. Geophys. Res.* 91, 385–401.
- Hawkins III, S.E., Boldt, J.D., Darlington, D.H., Espiritu, R., Gold, R.E., Gotwols, B., Grey, M.P., Hash, C.D., Hayes, J.R., Jaskulek, S.E., Kardian Jr., C.J., Keller, M.R., Malaret, M.S., Murchie, S.L., Murphy, P.K., Peacock, K., Prockter, L.M., Reiter, R.A., Robinson, M.S., Schaefer, E.D., Shelton, R.G., Sterner II, R.E., Taylor, H.W., Watters, T.R., Williams, B.D., 2007. The Mercury Dual Imaging System on the MESSENGER spacecraft. *Space Sci. Rev.* 131, 247–338.
- Hawkins III, S.E., Murchie, S.L., Becker, K.J., Selby, C.M., Turner, F.S., Nobel, M.W., Chabot, N.L., Choo, T.H., Darlington, E.H., Denevi, B.W., Domingue, D.L., Ernst, C.M., Holsclaw, G.M., Laslo, N.R., McClintock, W.E., Prockter, L.M., Robinson, M.S., Solomon, S.C., Sterner II, R.E., 2009. In-flight performance of MESSENGER's Mercury Dual Imaging System. In: Hoover, B., Levin, G.V., Rozanov, A.Y., Retherford, K.D. (Eds.), *Instruments and Methods for Astrobiology and Planetary Missions XII*. SPIE Proceedings 7441, paper 74410Z, SPIE, Bellingham, Washington, 12 pp.
- Howard, H.T., Tyler, G.L., Esposito, P.B., Anderson, J.D., Reasenbcrg, R.D., Shapiro, I.I., Fjeldbo, G., Kliore, A.J., Levy, G.S., Brunn, D.L., Dickinson, R., Edelson, R.E., Martin, W.L., Postal, R.B., Seidel, B., Sesplaukis, T.T., Shirley, D.L., Stelzried, C.T., Sweetnam, D.N., Wood, G.E., Zygielbaum, A.L., 1974. Mercury: results on mass, radius, ionosphere, and atmosphere from Mariner 10 dual-frequency radio signals. *Science* 185, 179–180.
- Montenbruck, O., Gill, B., 2000. *Satellite Orbits*. Springer, Berlin, 377 pp.
- Perry, M.E., Kahan, D.S., Barnouin, O.S., Ernst, C.M., Solomon, S.C., Zuber, M.T., Smith, D.E., Phillips, R.J., Srinivasan, D., Oberst, J., Asmar, S.W. Measurement of the radius of Mercury by radio occultations during the MESSENGER flybys. *Planet. Space Sci.*, this issue. doi:10.1016/j.pss.2011.07.022.
- Preusker, F., Oberst, J., Head, J.W., Watters, T.R., Zuber, M.T., Solomon, S.C. Stereo topographic models of Mercury after three MESSENGER flybys. *Planet. Space Sci.*, this issue. doi:10.1016/j.pss.2011.07.005.
- Robinson, M.S., Davies, M.E., Colvin, T.R., Edwards, K., 1999. A revised control network for Mercury. *J. Geophys. Res.* 104, 30,847–30,852.
- Röser, S., Bastian, U., 1991. PPM Star Catalogue. Positions and Proper Motions of 181731 Stars North of -2.5 Degrees Declination for Equinox and Epoch J2000.0, vols. 1 and 2. Spektrum Akademischer Verlag, Heidelberg, 1850 pp.
- Röser, S., Bastian, U., 1993. PPM Star Catalogue. Positions and Proper Motions of 197179 Stars South of -2.5 Degrees Declination for Equinox and Epoch J2000.0, vols. 3 and 4. Spektrum Akademischer Verlag, Heidelberg, 2011 pp.
- Smith, D.E., Zuber, M.T., Phillips, R.J., Solomon, S.C., Neumann, G.A., Lemoine, F.G., Peale, S.J., Margot, J.-L., Torrence, M.H., Talpe, M.J., Head III, J.W., Hauck II, S.A., Johnson, C.L., Perry, M.E., Barnouin, O.S., McNutt Jr., R.L., Oberst, J., 2010. The equatorial shape and gravity field of Mercury from MESSENGER flybys 1 and 2. *Icarus* 209, 88–100.
- Solomon, S.C., McNutt Jr., R.L., Gold, R.E., Domingue, D.L., 2007. MESSENGER mission overview. *Space Sci. Rev.* 131, 3–39.
- Solomon, S.C., McNutt Jr., R.L., Watters, T.R., Lawrence, D.J., Feldman, W.C., Head, J.W., Krimigis, S.M., Murchie, S.L., Phillips, R.J., Slavin, J.A., Zuber, M.T., 2008. Return to Mercury: a global perspective on MESSENGER's first Mercury flyby. *Science* 321, 59–62.
- Thomas, P.C., 1993. Gravity, tides, and topography of small satellites and asteroids: application to surface features of the Martian satellites. *Icarus* 105, 326–344.
- Thomas, P.C., Parker, J.W., McFadden, L.A., Russell, C.T., Stern, S.A., Sykes, M.V., Young, E.F., 2005. Differentiation of the asteroid Ceres as revealed by its shape. *Nature* 437, 224–226.
- Zuber, M.T., Smith, D.E., Solomon, S.C., Phillips, R.J., Peale, S.J., Head III, J.W., Hauck II, S.A., McNutt Jr., R.L., Oberst, J., Neumann, G.A., Lemoine, F.G., Sun, X., Barnouin-Jha, O., Harmon, J.K., 2008. Laser altimeter observations from MESSENGER's first Mercury flyby. *Science* 321, 77–79.